Phys. Status Solidi B **247**, No. 6, 1265–1281 (2010) / **DOI** 10.1002/pssb.200945514

physica status solidi b
www.pss-b.com
basic solid state physics

Self-organized growth of ZnO-based nano- and microstructures

Michael Lorenz[*,1], Andreas Rahm[1,2], Bingqiang Cao[1,3], Jesús Zúñiga-Pérez[1,4], Evgeni M. Kaidashev[1,5], Nikolai Zhakarov[6], Gerald Wagner[7], Thomas Nobis[1], Christian Czekalla[1], Gregor Zimmermann[1], and Marius Grundmann[,1]**

[1] Institut für Experimentelle Physik II, Universität Leipzig, Linnéstr. 5, 04103 Leipzig, Germany
[2] present address: Solarion AG, Ostende 5, 04288 Leipzig, Germany
[3] present address: School of Materials Science and Engineering, University of Jinan, 250022 Jinan, Shandong, P. R. China
[4] permanent address: Centre de Recherche sur l'Hétéro-Epitaxie et ses Applications, Centre National de la Recherche Scientifique, Rue Bernard Grégory, 06560 Valbonne, France
[5] permanent address: Mechanics and Applied Mathematics Research Institute, Southern Federal University, 344090 Rostov-on-Don, Russia
[6] Max-Planck Institut für Mikrostrukturphysik, Weinberg 2, 06120 Halle (Saale), Germany
[7] Institut für Mineralogie, Kristallographie und Materialwissenschaft, Universität Leipzig, Scharnhorststr. 20, 04275 Leipzig, Germany

Received 4 November 2009, accepted 22 December 2009
Published online 3 February 2010

PACS 73.21.Fg, 72.80.Ey, 78.67.Bf, 81.05.Dz, 81.16.Dn, 81.16.Mk

[*] Corresponding author: e-mail mlorenz@physik.uni-leipzig.de, Phone: +49 341 97 32661, Fax: +49 341 97 39286
[**] e-mail grundmann@physik.uni-leipzig.de; www.uni-leipzig.de/~hlp/, Phone: +49 341 97 32651, Fax: +49 341 97 32668

ZnO-based nano- and micro-structures with controlled orientation, size, and lateral density were grown by specially designed two-step pulsed laser deposition and direct carbothermal growth, respectively. Different substrate orientations and nucleation layers allow well-defined tuning of growth direction and lateral arrangement of the wires. As a result, axial MgZnO–ZnO nano quantum dots and homogeneous radial nano core-shell quantum well structures are demonstrated. Donor and acceptor doping of nano- and microwires influence considerably both electrical characteristics as well as morphology including branching. Field effect transistors with n- and p-type wire channel and nanowire p–n junctions seem to prove a reproducible p-type conductivity of phosphorous-doped ZnO wires.

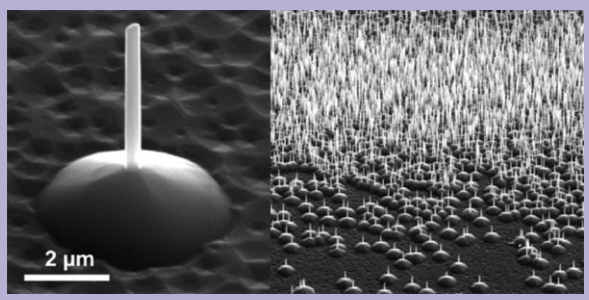

Single ZnO wire (309 nm thick, 3.99 µm high) grown on pyramidal base with controlled lateral density by tuning the ZnO template layer in a two-step PLD process.

1 Introduction The research interest in ZnO-based nanostructures has increased tremendously in the past decade due to the relative easiness to achieve a variety of self-organized, free standing nano- and microstructures. Review articles [1–8] cover the research directions pursued with regard to ZnO nanostructures, the envisioned applications and point to critical aspects on the way to novel optoelectronic nano devices. The main problem of current ZnO research is the high, reproducible, and stable p-type doping, as pointed out by Klingshirn [1]. We show later in this article that ZnO in micro and nanodimensions may offer decisive advantages in demonstrating reproducible p-type conductivity of ZnO. A competent overview on all aspects of ZnO bulk material, thin films, and nanostructures is given in Ref. [2]. A review on other materials with anisotropic structure besides ZnO with suitability to form one-dimensional nanostructures and their processing routes is given in Ref. [3]. ZnO nanowires with emphasis on sensing and

electrical nano device fabrication and demonstration of depletion mode transistors and Schottky diodes are reviewed in Ref. [4] and shortly in Ref. [5]. Self-organization and regularly patterned growth of semiconductor nanowires by nanosphere lithography are reviewed by Zacharias, Werner and Fan in Ref. [6]. The polar character of ZnO surfaces offers additional possibilities for sophisticated structures such as for example nanobelts, nanorings, and springs, as shown by Wang in Ref. [7]. Environment friendly methods for synthesis of nanostructures by application of green-chemistry principles are discussed. In particular, the molten-salt synthesis, hydrothermal protocols, and template-directed methods are considered as environmentally sound and cost effective [8].

Here, we describe the growth and characterization of ZnO-based nano and microstructure arrays, from selected single wires to more sophisticated core-shell nano quantum well (QW) structures. Furthermore, three independent indications for reproducible p-type conductivity of phosphorous-doped ZnO wires were found by acceptor-related luminescence lines, field-effect transistors (FETs), and p–n junctions. The ZnO wires are the materials base for optical excitation of optical modes and lasing and for coaxial nanowire Bragg resonators as described by Czekalla et al. and Schmidt-Grund et al., respectively, in this issue.

2 ZnO nanowire growth processes For the growth of ZnO-based micro- and nanowires, we have developed two physical growth processes, the direct carbothermal growth, and the two-step pulsed laser deposition (PLD), respectively. Concerning the atomistic growth process of nanowires using a metal template, traditionally the vapor-liquid–solid (VLS) growth is assumed to explain the experimental findings very well [9]. However, in particular for ZnO [10] and other materials as Ge [11] the morphology of the final wires points to more complicated growth models depending on the particular growth parameters, the temperature being most important. For ZnO a coexisting VLS and vapor-solid-solid (VSS) process [10] is assumed.

2.1 Direct carbothermal growth The scheme of carbothermal growth [12–14] is shown in Figure 1.

Table 1 shows the typical growth conditions for carbothermal growth of nanowires (diameter several 10 to 100 nm) and microwires (diameter several μm) in more detail. The main difference to grow nano- or microwires is the different process temperature, and the place where the wires grow. Nanowires grow on the substrate placed a few centimeter away from the source target in direction of Ar-flow, whereas thicker microwires grow directly on the source target as shown in Fig. 1. The direct carbothermal growth of ZnO microwires is also an ideal extension of the wire-diameter range covered by the high-pressure PLD, as described in Section 2.2.

The above mentioned coexisting VLS-VSS growth model for ZnO wires is further confirmed by Fig. 2, where

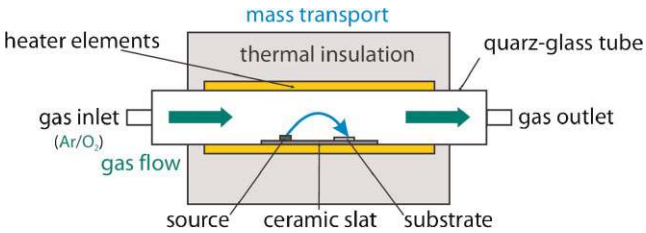

Figure 1 (online color at: www.pss-b.com) Setup of carbothermal evaporation. Nanostructures grow on the substrate by species transported in Ar gas stream, and thicker and longer microwires are formed directly on the ZnO:C source target at higher temperature, see Table 1.

Table 1 Conditions for carbothermal growth of ZnO nano- and microwires in tube furnace, see Figure 1.

parameter	nanowire growth	microwire growth
used substrate	sapphire, Si, GaN	no substrate
nucleation mater.	Au colloids 10 nm	ZnO:C source target
source target	ZnO:high purity graphite 1:1	
ZnO dopants	P, Mg, Sb, Ga, Al, Li	
gas flow	30 l/h Ar	air, open tube
gas pressure	1 bar	1 bar
growth temperature	870 °C	1,100 °C
growth time	30–120 min	30 min

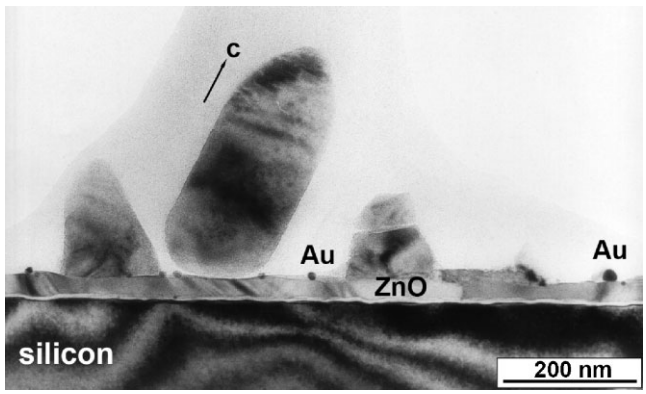

Figure 2 TEM bright field image of ZnO nanowires grown on Si (111) with Au nucleation layer by carbothermal evaporation. No Au droplets are seen on top of the wires, as expected for the VLS model.

the ZnO wires do not show any catalytic Au cap on top. The Au nucleation particles molten from the nm-thin sputtered Au layer are visible on top of the ZnO wetting layer formed on the Si substrate. Therefore, the ZnO nanostructure growth seems to be due to a VSS process rather than a VLS process (compare [10, 11]).

Figures 3 and 4 show high-resolution TEM cross-sections along and perpendicular to the ZnO *c*-axis, respectively. The wires were taken from the same sample as used in Fig. 2.

As expected from the nearly perfect ZnO wire structure demonstrated in Figs. 3 and 4, the nanowires grown by

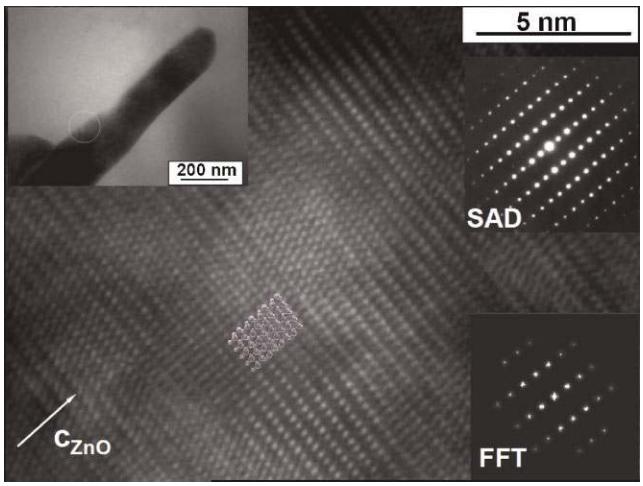

Figure 3 (online color at: www.pss-b.com) HRTEM lattice image of a ZnO wire on Si(111). Beam direction is parallel to [100] or [2-1-10]. Not any distortion of ZnO lattice is visible, confirming the nearly perfect ZnO single-crystal structure.

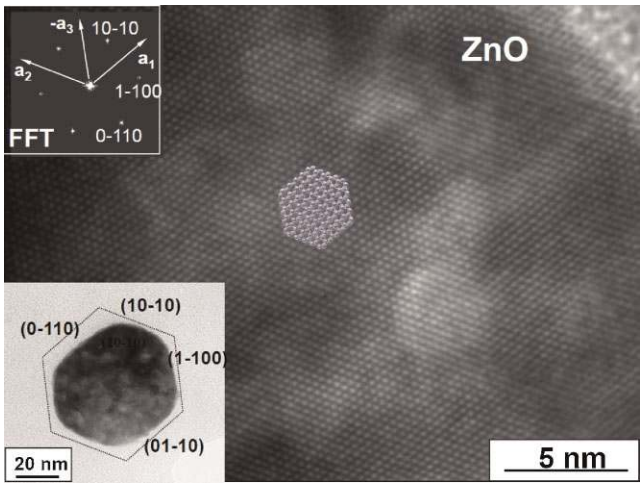

Figure 4 (online color at: www.pss-b.com) HRTEM lattice image of a ZnO wire on Si(111). Beam direction is parallel to [001] or [0001]. Again, not any structural defects can be seen.

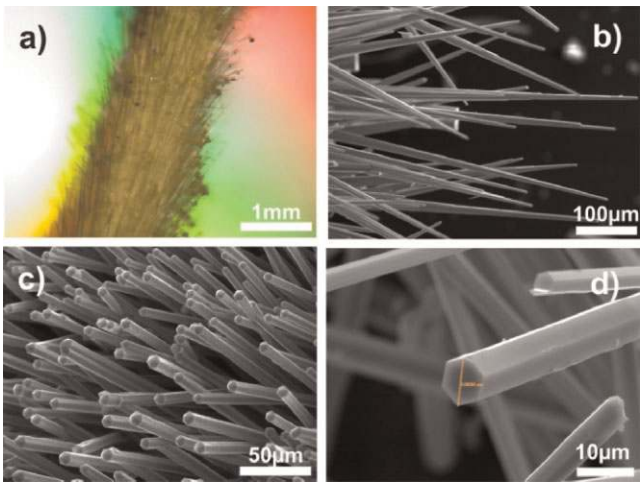

Figure 5 (online color at: www.pss-b.com) SEM images of ZnO-based microwires grown by carbothermal evaporation directly on the ZnO:C source target at 1,100 °C in air: (a) ZnO microwires at the edges of a macroscopic "tail", (b) tapered wires grown from ZnO+10 wt% P_2O_5: graphite target, (c) ZnO:P wires with pyramidal facets at the tips (d) hexagonal ZnO wire with 9.08 μm diameter.

carbothermal evaporation show very good luminescence properties as expressed by narrow cathodoluminescence (CL) widths of the donor bound exciton peak I_6 of only 1.1 meV at 10 K [15]. This value has to be compared with 1.2 meV for one of the best PLD ZnO films on a-plane sapphire and with 0.7 meV for a commercial Eagle-Picher ZnO bulk single crystal [15].

The influence of an addition of up to 1.5 wt% Al_2O_3 to the ZnO-graphite source target in carbothermal growth is described in Ref. [16]. The morphology changes from nanowires to free-standing, two-dimensional ZnO nanosheets, and branched honeycomb-like nanowalls together with one-dimensional nanothreads [16]. Section 3.4 shows other branched ZnO structures due to doping of the PLD target.

Figure 5 shows micrometer-thick ZnO microwires grown by the above described carbothermal growth directly on the source target. Figure 5 (a) shows a tail consisting of microwires starting from the source target. Figures 5 (b) and (c) show phosphorous-doped ZnO microwires as used for confirmation of p-type conductivity by back-gate field effect transistors (FETs) with microwires as channel [17, 18]. Doping of ZnO wires is described in more detail in Section 3.4 of this paper. Finally, Fig. 5 (d) shows a typical undoped ZnO microwire as used as optical medium for excitation of whispering gallery modes (WGMs) and lasing [19]. This work on WGMs has had high impact on the scientific ZnO community because our group was the very first one reporting on observation and modeling of WGMs in ZnO wires, as shown below and in the article by Czekalla et al. in this volume.

2.2 Two-step pulsed laser deposition PLD is an established physical deposition technique for a variety of thin film materials, in particular for oxides [20, 21]. In recent years, the application of PLD was extended to nanowire structures, and special setups were established for nanowire growth (see Refs. [21, 22]). PLD thin films show with increasing oxygen partial pressure during deposition above 0.2 mbar an increasing surface roughness [21]. Therefore, the idea to grow self organized nanostructures by PLD is to increase the background pressure to 100 mbar range, to use an inert (Ar) gas instead of the reactive oxygen, and a special growth reactor with controlled gas flow, see Refs. [22, 12, 13]. Figure 6 shows the scheme and the quartz reactor for

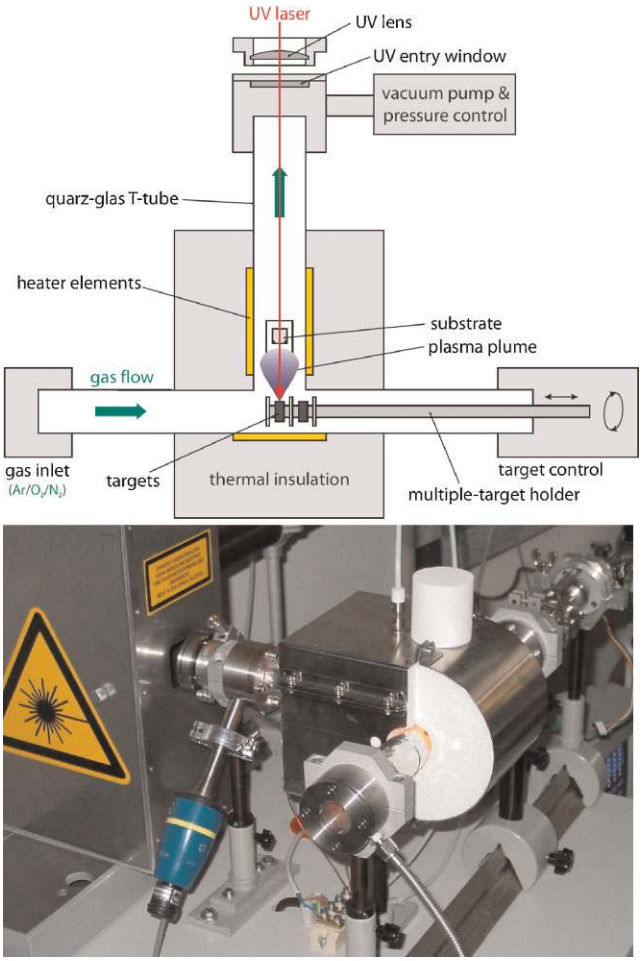

Figure 6 (online color at: www.pss-b.com) Scheme of high-pressure PLD chamber for growth of ZnO-based nano-heterostructures consisting of a T-shaped quartz tube with 30 mm outer diameter. Relative positions of rotating targets, plasma plume and substrate are also indicated. The laser beam is drawn red and the process gas flow green. Below is a corresponding photograph of the chamber operating at high temperature.

high-pressure PLD. Characteristic is the target-to-substrate distance of only 5 to 40 mm at about 200 mbar Ar pressure.

The high-pressure PLD is combined with a more conventional low-pressure PLD setup which is especially designed to grow nanowire core-shell structures or film-nanowire junctions in a two-step PLD process. Table 2 summarizes typical parameters for both the high-pressure (nanowire) and the low-pressure (film) PLD process. The capability of the high-pressure PLD for growth of ZnO nanowire arrays on single-crystalline *a*-plane, *m*-plane and *r*-plane sapphire, GaN-buffered Si(111), and SiC-4H substrates is demonstrated by Figs. 7–12, respectively. The PLD process allows for control of doping, wire diameter, aspect ratio, and lateral density of wires, as described below.

The growth direction of the ZnO wires is always [0001], but its orientation can be controlled by the underlying single-crystalline substrate.

On *a*-plane (11-20) (Fig. 7) and *c*-plane (0001) sapphire (not shown here), GaN (001) buffer layers (Figs. 10 and 11), and SiC-4H (Fig. 12), the ZnO films grow with the *c*-axis perpendicular to the substrate surface. On *r*-plane (1-102) sapphire (Fig. 9), the majority of wires are oriented in-plane, that means the *c*-axis is parallel to the substrate surface.

On *m*-plane (10-10) sapphire, the nanowires are inclined 30° with respect to the substrate normal (Fig. 8). The nanowires show well-defined epitaxial relationships with the *m*-plane sapphire substrate, the projection of the wires' [0001] axis being parallel to the in-plane sapphire [-12-10] direction [32].

The initial growth stages of PLD grown ZnO nanowires are depicted in more detail in Fig. 10, which shows two samples grown with only 500 and 2,000 laser pulses. The initial growth in the first several 100 laser pulses seems to follow the VLS model, but already after 500 pulses Au droplets begin to move down on the wire side facets toward the interface (Fig. 10 (b)). After 2,000 pulses, the further wire growth seems to proceed without any further participation of Au catalyst according to VSS model. Only few Au particles were found at and near the ZnO/GaN interface (Fig. 10 (c) and (d)). Fig. 11 shows ZnO wires on GaN-buffered Si(111) after 7,500 pulses.

The PLD-grown ZnO-based nanostructures are the materials base for a variety of state-of-the-art results, see Refs. [22–43]: Examples are donor and 3d-element doped wires [23, 29, 33, 38, 43], WGMs and lasing in nanowires [24, 26–28, 34, 35], ordered and tilted wire arrangements [30, 32], p-type doped nanowires and p–n junctions [36, 42], nanowire quantum dots and quantum wells [37, 41], and nanowall networks [39].

3 Application-related ZnO nanostructures

In the following sections, an overview is given on the ZnO nano and microstructures prepared specifically for special investigations as for example WGM excitation and lasing (Section 3.1), nanowire arrays with controlled lateral density (Section 3.2), axial and radial nano core-shell structures (Section 3.3), and finally p-type and n-type doped nanowires including nanowire FETs and p–n junctions (Section 3.4), see Refs. [12–43].

3.1 Single nano- and microwires for optical mode emission and lasing

Nominally undoped ZnO nano and microwires grown by high-pressure PLD were used to investigate WGMs in dielectric resonators with hexagonal [24, 26–28, 34] and also dodecagonal [35] cross-section.

Reference [24] presents first systematic investigations of WGMs in hexagonal resonators for small mode numbers. This work can be considered as the starting point of WGM investigation in hexagonal semiconducting nanowires with considerable impact on the international community.

Figures 13 and 15 show examples for nano and microwires, respectively, which showed WGMs in the spectral range of the ZnO visible defect band (the so-called green luminescence) by excitation with an electron beam in a

Table 2 Typical materials and deposition parameters for high-pressure and low-pressure "two-step" PLD growth of ZnO-based nano heterostructures.

parameter	high-pressure PLD	low-pressure PLD
grown structure	self-organized ZnO NW arrays	shells around NW core
used substrate	*a*-, *c*-, *r*-, *m*-sapphire, Si, SiC	nanowires, sapphire ZnO, Si
nucleation materials	Au colloids 10 nm, Au, Ni, ZnO films	N/A
ZnO dopants	Mg, P, Li, Al, Mn, Co	groups V, III, Mg, 3d elements
background pressure	50–200 mbar Ar	10^{-4}–1 mbar O_2
gas flow	50 sccm @100 mbar	N/A
growth temperature (typical)	420–940 °C (825 °C)	RT–780 °C (650 °C)
KrF laser	2 J/cm^2, 10 Hz	2 J/cm^2, 1–15 Hz
target–substrate distance (typical)	5–40 mm (8–20 mm)	25–80 mm (60 mm)

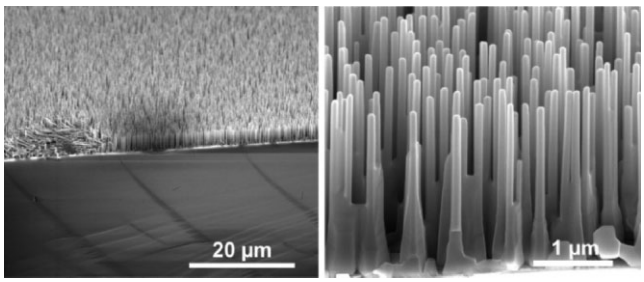

Figure 7 Lateral homogeneity of high-density undoped ZnO nanowire array grown on *a*-plane sapphire covered with 50 nm gold colloids at 860 °C and 100 mbar Ar-flow. The wires are 62–74 nm thick and 3.26–3.46 µm high, the aspect ratio being about 50. Images taken with a field emission (FE) scanning electron microscope (SEM) FEI Nanolab 200.

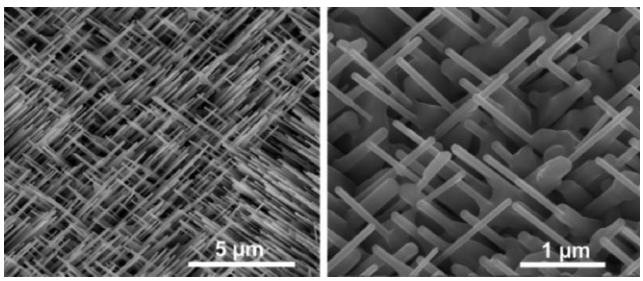

Figure 8 ZnO nanowire arrays grown on *m*-plane sapphire tilted by 30° to the substrate normal (see Ref. [32]).

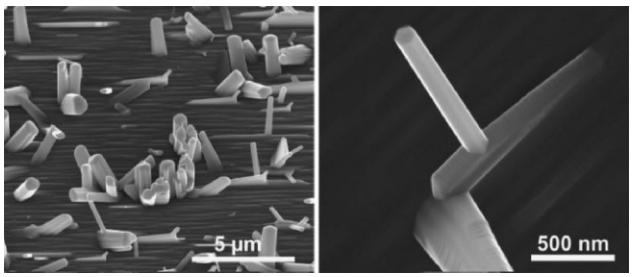

Figure 9 ZnO nanowires grown on *r*-plane sapphire. Typically, the ZnO *c*-axis is parallel to the substrate surface, but occasionally branched wires grow out of facets of the in-plane oriented wires.

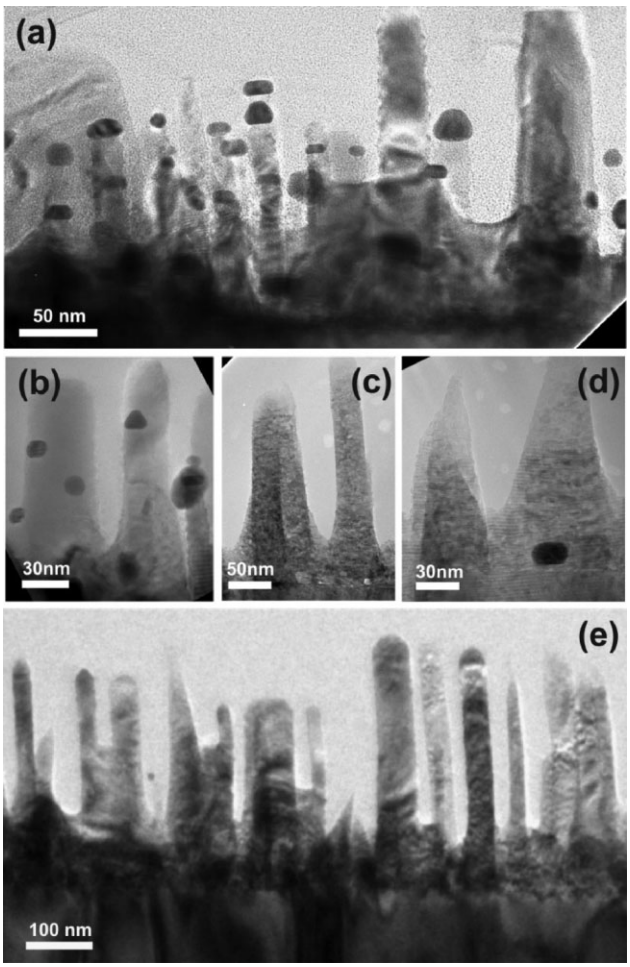

Figure 10 TEM images of the initial growth stages of PLD ZnO nanowires on GaN-buffered Si(111): (a) and (b) are taken after 500 laser pulses and show dark Au droplets on top of the wires (according to VLS model), and moving down on nanowire facets toward the interface. Images (c), (d), and (e) show a sample grown with 2,000 pulses. Not any Au is visible on top of the nanowires. Only few Au particulates appear near the bottom interface to the substrate (c) and (d). VSS seems to be the dominating mode. Growth was done at 840 °C and Ar flow at 100 mbar using a nm-thin sputtered Au nucleation film for both samples.

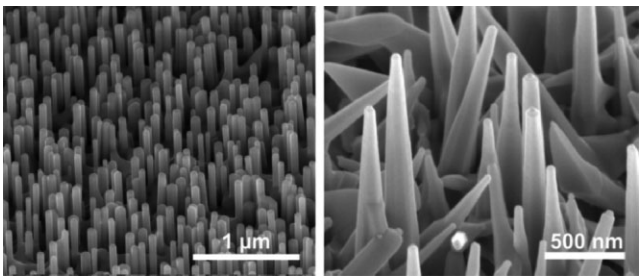

Figure 11 ZnO nanowire arrays grown on GaN (0001) buffered Si(111) using 7,500 laser pulses. GaN layers were grown by MOCVD by A. Dadgar, U Magdeburg. The tapered wires (right) were grown at increased distance 35 mm from target instead of 25 mm (left).

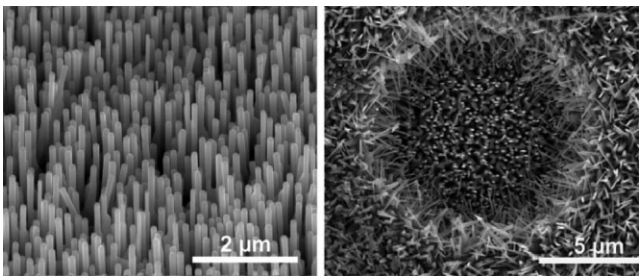

Figure 12 ZnO nanowires grown with their [0001] axis perpendicular to the surface of a SiC-4H single crystal substrate. The SiC-4H was supplied by G. Ferro, Université Lyon I, France. Right is a pinhole typical for single crystalline SiC.

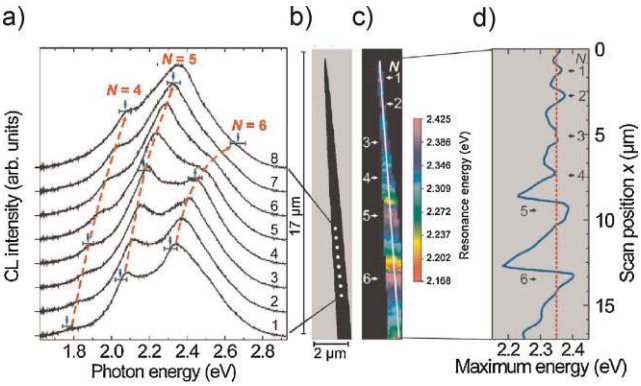

Figure 14 (online color at: www.pss-b.com) Spatially resolved CL investigation of a single tapered ZnO nanowire. (a) CL spectra shifted vertically for clarity collected at eight equidistant locations marked on the needle's longitudinal axis by white dots in (b). The visible band of ZnO between 1.8 and 2.9 eV is modulated such that maxima can clearly be distinguished from each other and attributed to WGMs. Since the radius of the needle decreases along the longitudinal axis, the spectral maxima continuously shift to higher energies as indicated by the red dashed lines. Blue arrows and error bars mark selected TM-resonance energies and their error. (b) Experimentally determined shape of the needle. (c) Map of the energy of the spectral maximum within the visible spectral range. (d) Line scan along the white line shown in (c). The red dashed line gives the maximum position of the unstructured visible band in bulk material. Image is taken from [24].

typical CL experiment. As a model system single, tapered, high aspect ratio zinc oxide nanoneedles were analyzed. These nanoneedles (Fig. 13) enabled systematic investigations as a function of the resonator diameter down to the nanometer regime down to mode number 1 (for details see in Fig. 14). Nanosized crystals show broadened WGMs due to the increase of losses with decreasing cavity diameter. A simple plane wave interference model without free parameter describes the spectral positions and the linewidths of the modes in good agreement with the experiment [24, 28].

Figure 15 shows microwires, whose cross-section changes from hexagonal at the bottom part to dodecagonal in the middle and top section. To analyze WGMs of such microstructures, polarization-resolved micro photoluminescence (µ-PL) spectroscopy was used [35]. The beam of a cw-HeCd laser is focused on the sample by a microscope objective to a spot of about 1 µm in diameter. The luminescence is collected by the same objective.

Figure 16 shows spatially resolved µ-PL spectra of the hexagonal/dodecagonal ZnO microwire as depicted in Fig. 15. The spatially resolved spectral µ-PL mapping in Fig. 16 clearly shows the transition from hexagonal to

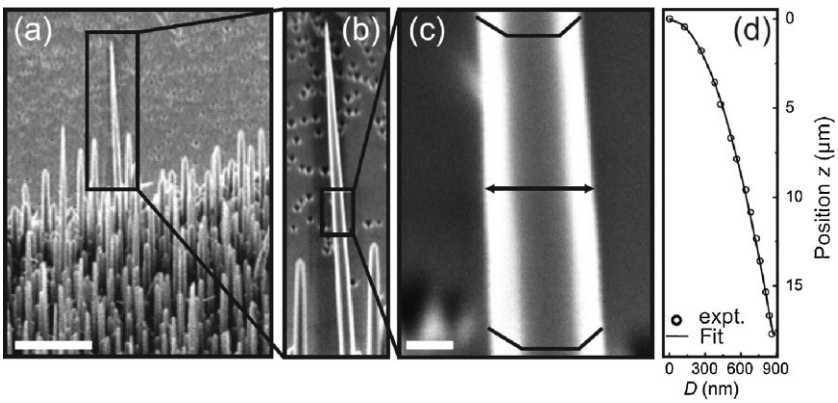

Figure 13 SEM images of a needle-like ZnO nanoresonator taken at 45° tilt angle. The scale bars correspond to (a) 10 µm and (c) 300 nm. The graph (d) is the experimentally determined shape of the needle. The wire diameter D is proportional to $z^{0.523\pm0.007}$, z being the axial position. Images were taken from [24, 28].

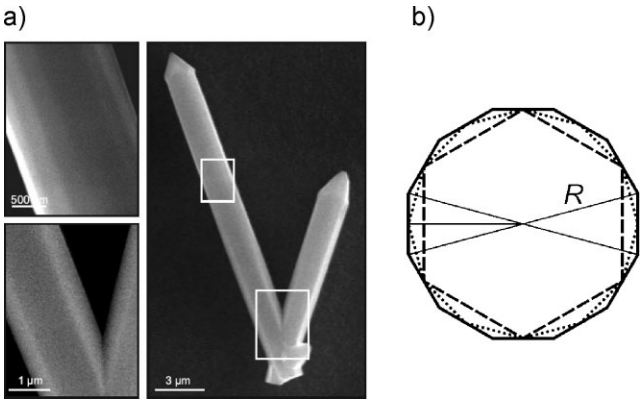

Figure 15 SEM images of a ZnO wire with changing shape from hexagonal at the bottom part to dodecagonal at the middle and top section (a). The images with higher magnification demonstrate the change of cross-section. (b) Inside of the dodecagon there is a dodecagonal (dotted line) and a hexagonal (dashed line) closed light path. Their total length is different. Image taken from [28].

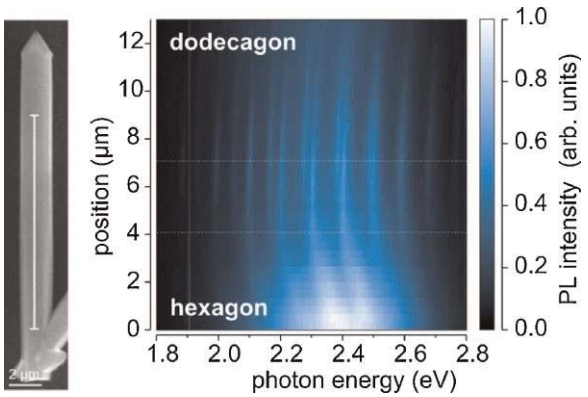

Figure 16 (online color at: www.pss-b.com) Spatially resolved µ-PL-spectra (spectral linescan) of the hexagonal / dodecagonal ZnO microwire shown in Fig. 15. Left is the SEM image of the wire with indicated position of the linescan. A series of PL spectra was taken along the white line, corresponding to the scan position in the right map. The horizontal axis is the photon energy of the luminescence. The color bar right gives the luminescence intensity. Bright curves show maxima of the spectral luminescence intensity, corresponding to the WGM modes. The change from hexagonal to dodecagonal cross-section is in between the two horizontal dotted lines. Narrow, fixed lines at 1.9 and 2.1 eV are side bands of the exciting HeCd laser. Image taken from Ref. [28].

dodecagonal cross-section in between the two horizontal dotted lines.

Lasing phenomena benefit from the larger cavity length of microwires, as compared to nanowires, making it easier to overcome the large mirror losses. ZnO microwires are usually hexagonally shaped, giving rise to another type of cavity: the WGM type of lasing. Here, the light wave circulates around within the hexagonal cross-section of the wire due to total internal reflection at the resonator's boundaries. Whispering gallery mode lasing has been

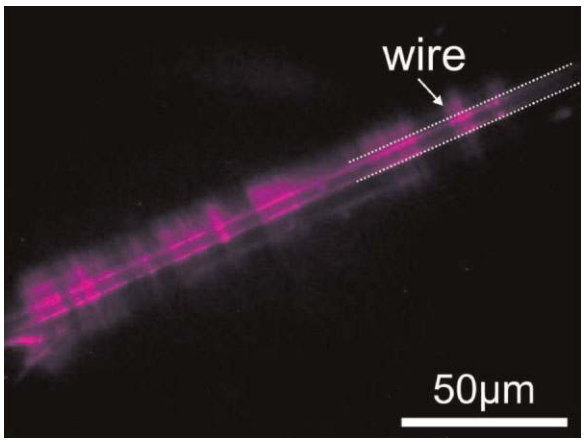

Figure 17 (online color at: www.pss-b.com) Optical microscopy image of the radial WGM lasing of an optically pumped microwire. The angle of incidence of the exciting laser beam is approximately 60° to the surface normal of the substrate. The excitation spot is much larger than the wire length, therefore the excitation intensity is regarded to be homogeneous over the entire microwire. The digital camera detects near UV radiation of the radially emitted WGMs. The diameter of the wire is indicated by the dotted lines as guide to the eye.

observed from single ZnO microwires grown by direct carbothermal evaporation (see Ref. [19] and references therein).

The emission of the radial WGMs is visualized in Fig. 17. The used microwires have diameters in the range between 1 and 20 µm. The microwires show a high PL signal under low excitation conditions. The number of observed peaks increases with increasing excitation intensity and the peaks show a highly superlinear dependence of the emitted intensity on the excitation intensity, a clear indication for lasing. The energetic position of the lasing peaks suggests the electron hole plasma as a gain mechanism [19].

We attribute the observed peaks to WGMs. The energetic peak positions were calculated from a simple plane wave model [19, 24, 28]. The model fits the experimental results very well. The full width at half maximum (FWHM) of the lasing peaks decrease with increasing wire diameter in good agreement with theory of hexagonal cavities. For 3 µm thin wires, we observe a FWHM of 1.3 meV. For wires larger than 7 µm in diameter, the observed FWHM is 0.6 meV, close to the spectral resolution of our setup [19]. Further details about WGM mode lasing and the corresponding models can be found in the references and the article by Czekalla et al. in this issue.

3.2 Nanowire arrays with controlled lateral wire density ZnO nanowire arrays with low lateral density of the nanowires are necessary for the growth of radial ZnO-based QW heterostructures (see Section 3.3) and also to grow coaxial Bragg resonators around ZnO nanowires (for more details see article of Schmidt-Grund et al. in this issue). In order to reduce the nanowire's area density, a novel two-step PLD method was developed for growing a ZnO

buffer layer and the ZnO core nanowires. This enables us to reduce the density of the nanowires to levels below 0.1 NW μm^{-2} [41].

The synthesis of the low density wires was carried out successively in two PLD chambers, the high-pressure quartz glass PLD chamber for the nanowire growth, and a conventional (low-pressure) PLD chamber for the initial nucleation layer growth and for a possible later shell growth.

First, a ZnO layer of about 250 nm was deposited on *a*-plane sapphire substrates using the conventional PLD chamber at a background oxygen pressure of 0.02 mbar and at a temperature of about 650 °C. Then, those ZnO layers were transferred into the high-pressure PLD chamber for the nanowire growth. The KrF laser repetition rate was set at 10 Hz and the laser energy density on the target was about 2 J cm^{-2}. The distance from target to the front edge of the substrate was 5 mm. Figure 18 shows the direct influence of the ZnO nucleation layer thickness on the lateral density of the nanowire arrays.

The growth of ZnO nanowires by high-pressure PLD on sapphire, with or without intentional metal catalyst on the substrate surface, leads to the growth of high density nanowire arrays of the order of ~10 nanowires μm^{-2}, as shown in Fig. 18 (b) and (d). If we take into account the nanowire mean diameter (typically between 100 and 150 nm), this density leads to a surface area coverage of the order of 10–20%. Under these conditions, the growth of homogeneous core/shell structures is not possible by PLD due to a strong shadowing effect by neighboring nanowires as depicted in Ref. [41].

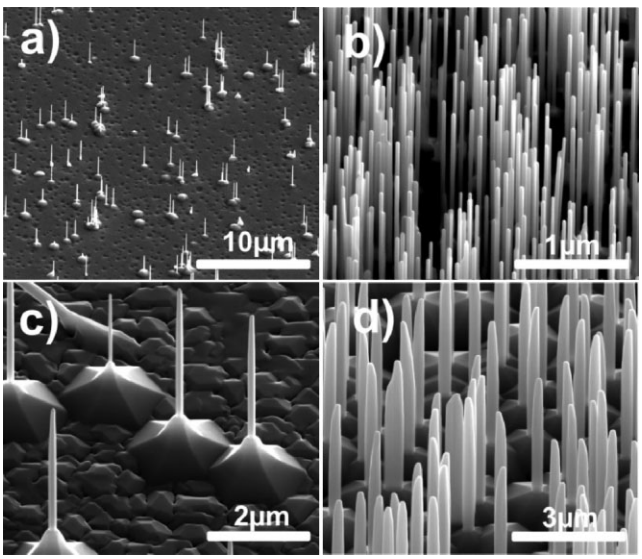

Figure 18 Overview on ZnO nanostructures grown by high-pressure PLD at 50 sccm Ar-flow at 100 mbar pressure and about 780–830 °C growth temperature on *a*-plane sapphire substrates: a, b) ZnO wires with low (a) and high (b) lateral density grown on *a*-sapphire with thick (>100 nm) and very thin (residual) ZnO nucleation layer, respectively. Obviously, the thickness of ZnO nucleation layer controls the lateral wire density. (c) Low-density 160 nm thick and 3.3 μm long ZnO wires grown on MgZnO nucleation film at reduced growth temperature of 780 °C. (d) ZnO wires with about 330 nm diameter and 4.5 μm height grown in the intermediate ZnO–sapphire region defined by the edge of substrate holder. ZnO nucleation layer is very thin in this sample area. See also the abstract figure.

The described shadowing effect can be avoided by reducing the area density of nanowires to levels at which the incoming beams (either plasma, molecular, or atomic) are not masked by any of the surrounding nanowires. We have achieved this by introducing a ZnO buffer layer, some hundreds of nanometres thick, grown by low-pressure PLD.

Figures 18 (a) and (c) show that we can obtain densities below 0.1 nanowires μm^{-2}. As will be shown in the following, this is low enough to prevent any shadowing effect. Indeed, the nanowire density varies continuously from the high density on sapphire to the low density values on the ZnO film. In between there is a transition region that has a lateral extension of ~100 μm and where the ZnO buffer layer thickness varies gradually (as the nanowire density, see Fig. 18 (d)). In order to understand the role of the ZnO film on reducing the nanowire density, we have measured its thickness by ellipsometry prior to and after the nanowire growth. It comes out that the incoming ZnO incorporates much more effectively into the ZnO buffer film than into the film growing in between the nanowires on the bare sapphire region: in this region, the ZnO film grown in between the nanowires is just some tens of nanometres thick, whereas in the region with the buffer ZnO film its thickness increases by about 500–1,000 nm, depending on the measurement position along the PLD plasma plume. This preferential incorporation into the ZnO buffer film seems to prevent nanowire nucleation and growth, since not only the nanowire density is reduced but also the pyramids that are found at the bottom of most of the nanowires (Fig. 18). Even though under all the experimental conditions investigated in this study the presence of the ZnO film drastically reduces the nanowire density, it is still unclear whether other parameters, such as the film roughness, could modify the nanowire density and thus allow further tuning.

After the growth of the low density nanowires, the samples will be transferred back to different low-pressure PLD chambers for the shell growth. The shell can be either a nano-QW structure (see below), or a coaxial Bragg resonator (see Schmidt-Grund et al.). In general, the growth conditions of the shell structure are similar to those employed for the ZnO layer growth with the only difference that for the growth of the QW, the laser repetition rate was reduced from 10 to 5 or 2 Hz. The low-pressure chamber to grow the coaxial Bragg resonators was initially designed for the flexible growth of large-area high-T_c superconducting thin films and allows a continuous tilt of the substrate heater with respect to the plasma plume. This substrate tilt and rotation during PLD is the key issue to achieve homogenous coaxial Bragg mirrors around the free standing ZnO nanowires with well-controlled thickness. These nanowires surrounded by radial Bragg reflectors are used as nano-resonators for optical investigations of strong exciton–photon coupling.

3.3 Axial and radial nano core shell structures In this section, the growth of axial and radial core–shell structures is described. First, the growth of axial films of MgZnO/ZnO/MgZnO on top ZnO nanowires resulted in quantum dot-like (QD) structures with highly spatially dependent quantum-dot like luminescence emission. Second, the growth of more homogeneous axial and radial core-shell nano QWs on low-density nanowire arrays is demonstrated.

3.3.1 Quantum dots in nanowires In order to achieve photonic ZnO nanowires devices, the implementation of heterostructure technology to the well established nanowires growth process and especially the incorporation of QWs and QDs is of current interest, as already shown for InAs/InP structures and for nanowire InGaN/GaN QWs (see Ref. [37] and references therein). Compared to GaN, ZnO offers the advantage of a higher exciton binding energy, allowing the observation of excitonic effects at room temperature. Recently, indications for embedded ZnO QDs were found in axial ZnO/MgZnO multiple QW structures, showing an additional peak in low-temperature photoluminescence spectroscopy [44]. In single ZnO/MgZnO QWs on top of isolated nanowires, the usually broad QW emission band consisted of two sharp and polarization dependent peaks in near-field PL [45] with line widths between 3 and 12 meV.

Axial MgZnO/ZnO QWs have been grown on top of high-density ZnO nanowires by PLD [37]. The ZnO nanowire arrays and the MgZnO/ZnO/MgZnO QWs on *a*-plane sapphire substrates were grown by two-step PLD. Both *in situ* processing within one chamber or *ex situ* growth in two different chambers was used [37]. At first, a high-pressure PLD process running at 75–100 mbar Ar partial pressure was used to grow undoped ZnO nanowire arrays on *a*-plane sapphire substrates. Ten nanometer gold colloids were employed as nucleation sites. Secondly, the MgZnO barriers from $Mg_{0.1}Zn_{0.9}O$ targets and the ZnO QW were grown on top of the nanowire arrays. The oxygen partial pressure for the barrier growth was 0.016 mbar and the growth temperature 670 °C. On top of the ZnO nanowire arrays, 200 laser pulses (25 nm) ZnO buffer layer, 600 pulses (80 nm) MgZnO bottom barrier, 11–17 pulses (2 nm) ZnO QW, and finally 250 pulses (30 nm) MgZnO top barrier were grown. All thicknesses are approximate values corresponding to the number of growth pulses.

Optical emission originating from the MgZnO barrier and the ZnO QDs was observed up to room temperature. Figure 19 shows CL intensity images for the emission energies of bulk ZnO (wire body), ZnO QW, and MgZnO barrier. It can be seen clearly that barrier and QW were only grown on top of the nanowires and that no lateral growth has taken place.

From comparison of the energetic position of the MgZnO band with thin film results, the Mg content is about 28% in the MgZnO barrier [46]. From the average position of the QW emission, the QW thickness can be determined to be around 2 nm [47]. Furthermore, the QW emission is not

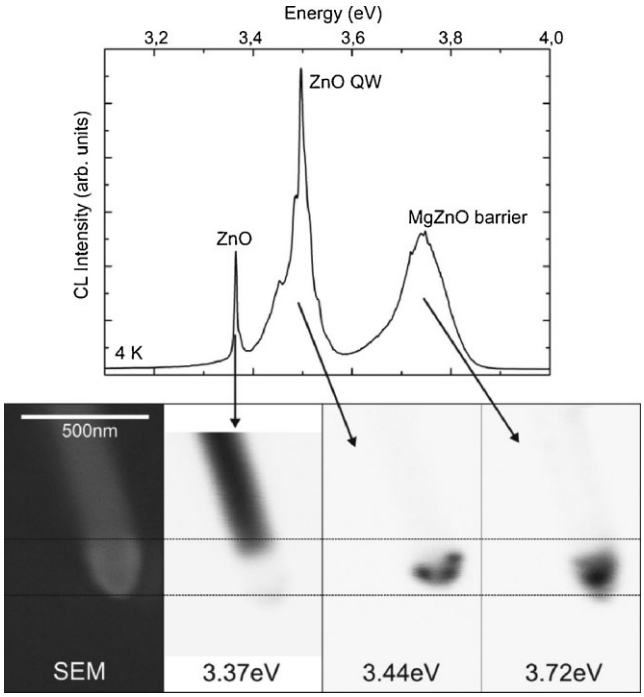

Figure 19 CL intensity images and the related SEM picture of the top of a single nanowire at 4 K. A typical low temperature CL spectrum averaged over the top region of the wire is shown. The intensity images show the spatial distribution of the CL signal for three different spectral regions corresponding to ZnO bulk, QW, and MgZnO barrier as indicated. The QW and the MgZnO barrier are located only at the top end of the wires. In contrast to this, the ZnO signal is detected from the wire body. There is no QW or MgZnO signal away from the top; thus, it is evident that no lateral (radial) growth of the barrier material was realized.

homogeneously distributed over the top of the wire. Instead of a single QW region, the CL intensity images show several areas of higher CL emission. Indeed, ensembles of spatially fluctuating and narrow CL peaks with individual widths down to 1 meV are found at the spectral position of the QW emission at 4 K as shown in Fig. 20. The spectra in Fig. 20 were taken at four positions a few tens of nanometers apart. The number of those peaks increases with increasing photoluminescence excitation, thus pointing to QD-like recombination centers on top of the nanowires [37].

By means of high resolution transmission electron microscopy, laterally strained areas of about 5 nm diameter were identified at the QW positions on top of the nanowires (Fig. 21). For some of these areas, corresponding dislocations were found in the inverse fast Fourier transformation images Fig. 21 (c) and (d). Consequently, the strain may be attributed to heavier ZnO nano QWs embedded in the lighter MgZnO matrix. This is in good agreement with the CL results.

3.3.2 MgZnO–ZnO quantum wells in nanowires By using high-pressure PLD on sapphire substrates, ZnO nanowires with a density in the order of 10 nanowires

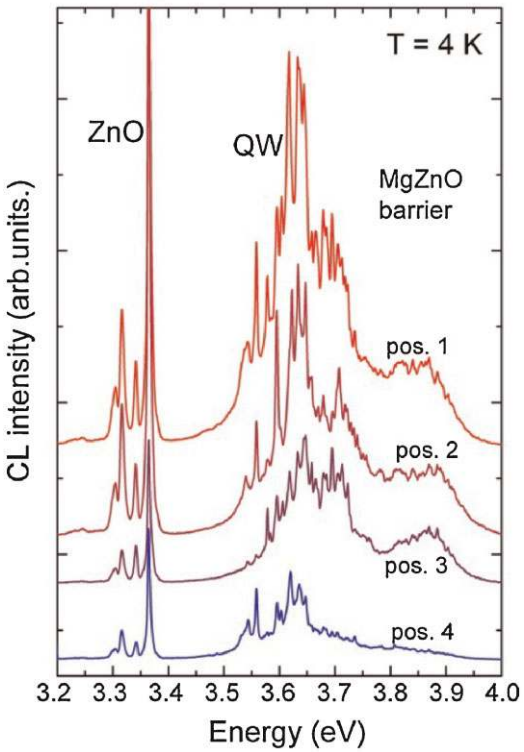

Figure 20 (online color at: www.pss-b.com) Strong dependence of low temperature CL spectra on electron beam spot position on top of a single selected nanowire with QW structure. Here, an *in situ* process within one PLD chamber was used for the wire and QW growth. The wire diameter was 2 μm. The spectra were taken at positions a few tens of nanometers apart. The Mg content of the ZnMgO barriers is 28%.

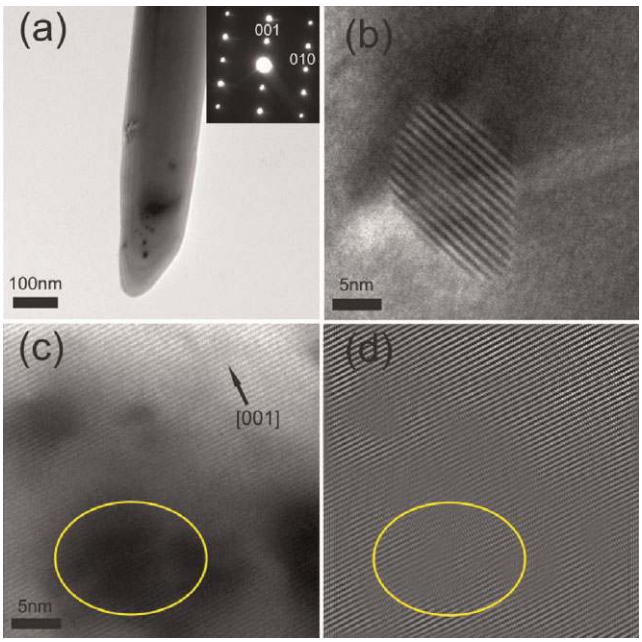

Figure 21 (online color at: www.pss-b.com) (a) Bright-field image of the upper part of a ZnO nanowire and associated SAED pattern (inset). (b) Moiré fringes produced by a nanocrystallite embedded into the surrounding matrix. (c) HRTEM image near the tip of the nanowire showing a dark area and (d) corresponding IFFT image showing the dislocations inside this area. Images were taken by N. Boukos and A. Travlos, National Center for Scientific Research Demokritos, Greece.

per μm^2 are obtained. If under these conditions ZnO/ZnMgO heterostructures are grown, only axial heterostructures can be obtained due to the large shadowing effect by neighboring nanowires. In this case the Mg content is modulated along the longitudinal growth direction, i.e., along [0001], as described above [37]. Thus, in order to obtain radial heterostructures by PLD, the lateral nanowires density has to be reduced. Therefore, we have introduced either a ZnO or a ZnMgO buffer layer by low-pressure PLD prior to the growth of ZnO nanowires by high-pressure PLD, as shown in Section 3.2.

The homogeneous growth of the QW shells on the low-density ZnO nanowires is demonstrated in Fig. 22, where the shell growth is monitored for one selected nanowire. Due to the shell growth, the thickness of the structure has increased considerably. By this identification of single nanowires and comparing their heights and diameters before and after the shell deposition, the axial to radial growth ratio was measured. Under typical low-pressure PLD growth conditions, the axial to radial growth rate ratio can vary from 3 to 7 [41]. This means that the top shell and, eventually, the axial QWs, will be thicker than the radial shell and QWs.

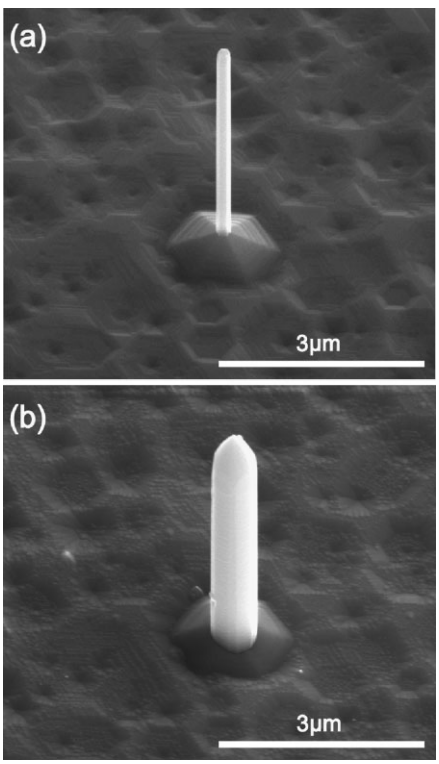

Figure 22 SEM images (recorded at a 45° tilt angle) of exactly the same nanowire (a) before and (b) after the shell growth [41].

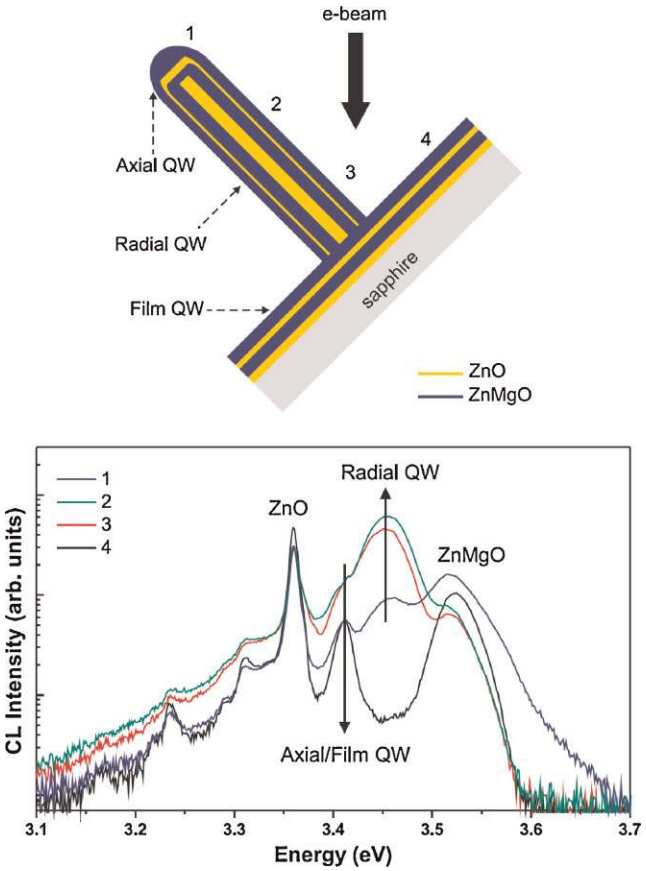

Figure 23 (online color at: www.pss-b.com) Schematic diagram of a single ZnO/ZnMgO QW wire as oriented in the CL cryostat, and CL spectra ($T = 10$ K, $U = 15$ kV, $I = 150$ pA) measured at the locations indicated on top [41].

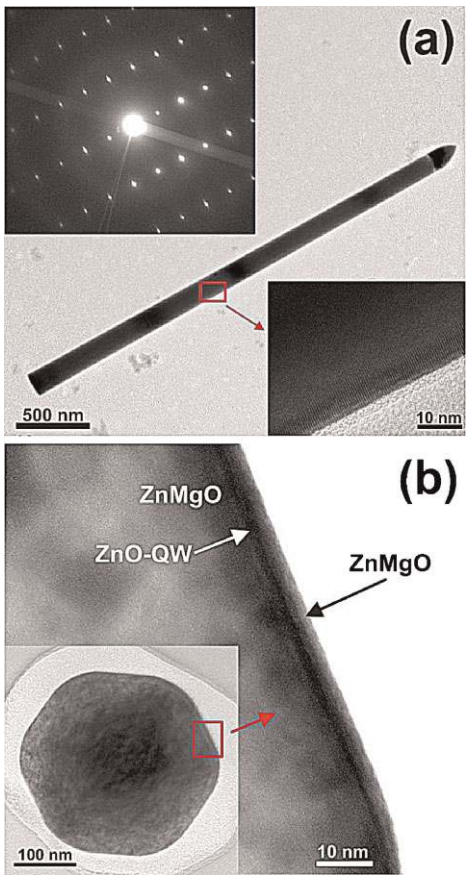

Figure 24 (online color at: www.pss-b.com) (a) TEM image of a ZnO/ZnMgO QW nanowire perpendicular to its longitudinal axis. The insets show SAED pattern taken from the body of the nanowire and high resolution TEM image taken from the sidewall. (b) TEM image of a ZnO/ZnMgO QW nanowire with the electron beam parallel to its longitudinal axis. The radial ZnMgO/ZnO/ZnMgO QW can be observed. The inset shows a general view of the nanowire transverse section. Images taken by N. Boukos and A. Travlos, adapted from Ref. [41].

The samples contain, therefore, not only the radial QW but also at least two more QWs. As schematically shown in Fig. 23 (top), these additional QWs are found at the tip of the nanowires and on the ZnO buffer layer. Their thickness will be larger and, thus, their emission energy will be found below that of the radial emission. For confirmation of the origin of each of the peaks in between the near-band-edge emissions of ZnO and ZnMgO, we have measured low-temperature CL spectra at different locations along the nanowire's longitudinal axis, as well as on the surface of the buffer layer close to the nanowire (Fig. 23, bottom). Obvious is the appearance of two additional peaks, at 3.45 and 3.41 eV, in between the emission of the ZnO core and the ZnMgO barrier. Two features are to be noticed: first, the intensity ratio of the 3.41 to 3.45 eV peak increases at the tip of the nanowires with respect to the center of the nanowires; second, when the CL spectra are recorded on the film, the emission at 3.45 eV vanishes completely and only the emission at 3.41 eV is observed. Both facts lead to the conclusion that the emission at 3.45 eV originates from the core/shell QW and the emission at 3.41 eV from the axial one, either at the nanowire tip or on the surface of the buffer layer. Furthermore, in the CL spectrum measured at the center of the nanowire (position 2 in Fig. 23, top) the emission from the axial/film QW is observed as a shoulder in the low energy side of the radial QW. This can be simply explained by exciton diffusion from the position where the CL is excited toward these QW and is consistent with recent measurements of exciton diffusion length in ZnO-based nanowires.

TEM images in Fig. 24 show that the nanowires are either defect-free or contain, in some cases, basal stacking faults perpendicular to the axial growth direction. SAED on the ZnO nanowires confirmed that the axial growth direction is parallel to the *c*-axis. High resolution TEM on the regions near the sidewalls shows well-defined ZnO/air interfaces with no observable roughening or {10.11}-type nanofacets, which could hinder the formation of homogeneous shells. Indeed, as shown in Fig. 24(b), the growth of the ZnO QW occurs homogeneously around the whole nanowire perimeter and the QW is even continuous at the 60° corners in passing from one {10.10}-type sidewall to the next one.

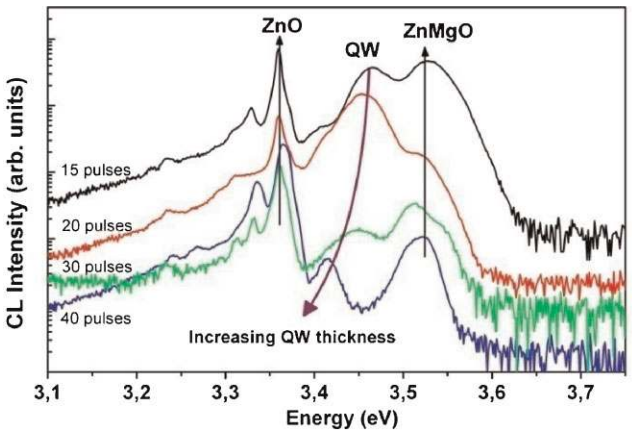

Figure 25 (online color at: www.pss-b.com) CL spectra ($T = 10$ K, $U = 15$ kV, $I = 150$ pA) measured from four different single ZnO/ZnMgO QW nanowires with different QW thicknesses (15, 20, 30, and 40 PLD pulses). The spectra are shifted vertically in intensity for clarity. Image was taken from [41].

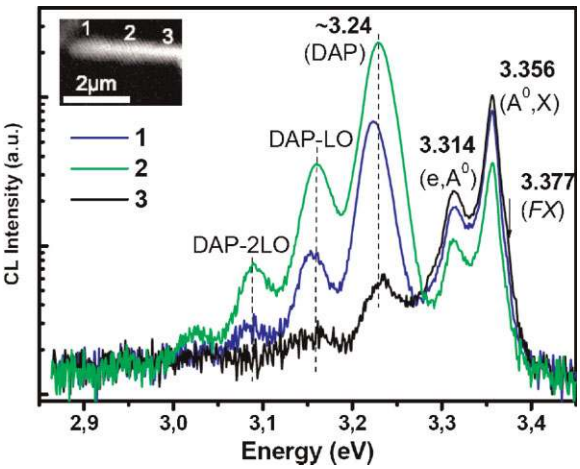

Figure 26 (online color at: www.pss-b.com) Low-temperature CL spectra of a phosphorous doped ZnO nanowire, indicating typical acceptor-related peaks (A^0,X), (e,A^0), and DAP (peak energies given in eV) of the phosphorous-doped wire.

However, it seems that the QW thickness varies slightly from the center of the {10.10} plane to the region closest to the corner. This continuity of the QW in passing from one {10.10}-plane to the next one is facilitated by the smearing out of the 60° corner due to the deposition of the inner ZnMgO barrier. The effect, by which Mg incorporation leads to the transformation of hexagonal ZnO nanowires into rounded ones, has been recently explained in terms of differences in {10.10} and {11.20} surface energies together with unequal energy gain due to Mg adsorption on those two crystallographic planes [48].

Figure 25 shows a series of core/shell QWs grown with varying well thickness. The CL spectra, obtained at the center of the nanowires (corresponding to position 2 in Fig. 23), show a redshift of the QW emission when larger QW thicknesses are measured. This systematic shift, due to quantum confinement, shows that controlled tuning of the radial QW energy has been achieved and proves the reliability of our proposed methodology for achieving homogeneous core/shell heterostructures with physical deposition methods.

3.4 Doped ZnO nanowires This final section deals with the growth of p-type and n-type doped ZnO nano- and microwires. The incorporation of acceptor or donor elements may influence the nanowire growth considerably, as shown by examples of branched nanostructures. p-type conductivity of ZnO is one of the major challenges, because long-term stable, reproducible, and easy p-type conducting ZnO thin films could not obtained up to now [2, 49, 50]. We present in the following three independent indications for p-type conductivity of phosphorous doped ZnO nano- and microwires. First results on e-beam lithography and electrical characterization of n-type doped ZnO nanowires are presented at the end.

3.4.1 p-type ZnO:P wires We use both high-pressure PLD and carbothermal evaporation to grow ZnO-based nano- and microwires, respectively. By simply adding P_2O_5 into the source targets of both processes, phosphorous-doped ZnO nano- [36] and microwires [17] could be grown successfully. CL spectra of single selected ZnO:P nano- and microwires show acceptor-related peaks (A^0,X), (e,A^0), and DAP, as demonstrated in Fig. 26 for ZnO nanowires [36]. Similar acceptor-related peaks were detected for phosphorous-doped ZnO microwires [17]. The assignment of the acceptor-related peaks was further confirmed by temperature-dependent CL spectra and appropriate fits of the peak energy shifts and by spatial CL maps individually extracted for selected peaks, as discussed in detail in Ref. [37].

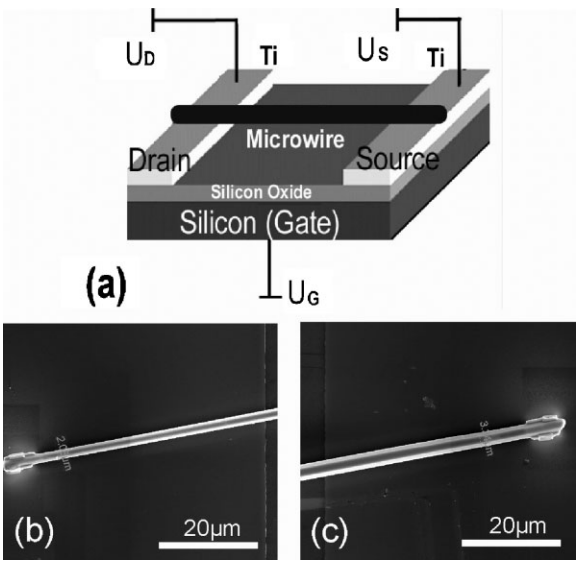

Figure 27 (a) Scheme of the bottom-gate microwire FETs. (b) and (c) SEM images of the source and drain contacts (made by IBID) of an undoped ZnO microwire channel with diameter of 2–3 μm. The total length of the microwire channel is 334 μm.

In order to confirm the conductivity type of undoped (intrinsically n-type) ZnO and ZnO:P microwires, they were used as channels in bottom-gate FETs. The microwires with length of several 100 μm were used for this purpose, because the usual tungsten contacts prepared by ion-beam induced deposition (IBID) do not allow the use of μm-short nanowires. The FETs were built on Si (100) substrates with a thermally grown, 190 nm thick SiO_2 gate oxide layer, as shown schematically in Fig. 27.

Three-terminal, gate voltage dependent electrical measurements of back-gate FETs with the microwires as channels indicate reproducibly for more than 10 samples that undoped and phosphorous-doped ZnO:P microwires are n-type and p-type conductive, respectively. This is demonstrated by the opposite source–drain current (I_{SD}) vs. gate voltage (U_G) transfer characteristics of undoped and P-doped wires, as shown in Fig. 28. The p-type conductivity of the ZnO:P microwires was found to be stable over more than 6 months.

As direct Hall measurements on nanowires are difficult since the necessary 2D configuration of the Hall contacts is hard to achieve, a third method to investigate the conductivity type of the ZnO:P nanowires are p–n junctions built from ZnO:Ga films and ZnO:P nanowires grown on top of the n-type conducting films. These p–n junctions were grown by two-step PLD on *a*-plane sapphire substrates. On the top of these n-type films, phosphorous-doped ZnO (ZnO:P)

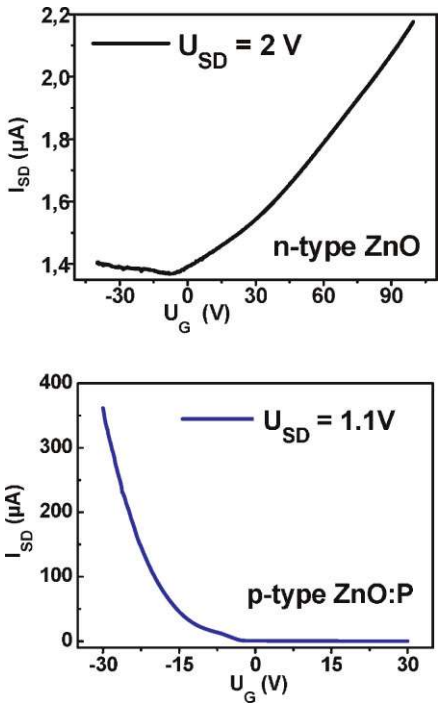

Figure 28 (online color at: www.pss-b.com) Typical opposite I_{SD} vs. U_G transfer characteristics of bottom gate FETs built *top* with undoped (n-type) and *bottom* with phosphorous-doped (p-type) ZnO microwires as channel. The channel depletion is obtained for negative or positive gate voltage, indicating n-type or p-type conductivity, respectively.

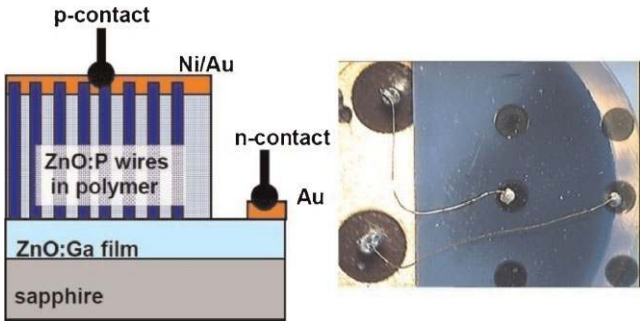

Figure 29 (online color at: www.pss-b.com) Scheme of the ZnO:P nanowire / ZnO:Ga film p-n-junctions grown on *a*-plane sapphire substrate including the p- and n-contact. Right is a top view of a typical transparent junction structure on TO-39 socket with contact wires connected to two wire top contacts.

nanowires were prepared by high-pressure PLD. For typical growth parameters see Table 1 and Ref. [42]. Figure 29 shows the scheme of the ZnO junctions and the arrangement of p- and n-contacts. The ZnO:P nanowires were embedded in polystyrene to allow well defined contacts to the tips of the ZnO:P nanowires, as shown in Fig. 30. Prior to evaporation of the Ni/Au contacts, the nanowire tips are treated with an oxygen plasma to remove residual polystyrene.

The ohmic behavior of the Au-ZnO:Ga contacts was proved by linear *I–V* curves through an Au-ZnO:Ga-Au arrangement [42]. The series resistance of the two involved n-contacts together with the ZnO:Ga film is only about 15 Ω. To check the Ohmic behavior of the p-contacts to the ZnO:P nanowires in the same way is not feasible as the wires are connected only vertically to the n-type ZnO:Ga film. Therefore, we could measure the current through two oppositely arranged p–n diodes, which is the p1–n–p2 configuration in Fig. 31. As for both positive and negative voltage always one diode is in reverse direction, the p1–n–p2 *I–V* curve is determined for both polarities by the leakage current of the reversely biased one of the two diodes. Figure 31 shows also the single junction *I–V* curves p1–n and p2–n of the two particular diodes. Indeed, the reverse parts of the *I–V* curves of all three curves (p1–n, p2–n, and p1–n–p2) in Fig. 31 agree reasonably well. The clearly rectifying *I–V* curves of the single junctions p1–n and p2–n are typical curves obtained similarly for more than 35 such p-n junctions on 13 samples [42]. This, in addition to the acceptor related CL peaks [36, 17] and the opposite FET transfer characteristics [17], is a

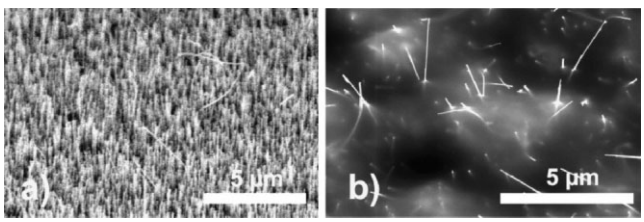

Figure 30 Scanning electron microscope images of ZnO:P nanowire array on a ZnO:Ga sample: (a) as grown, (b) after polystyrene embedding and plasma-etching the tips of the ZnO:P wires.

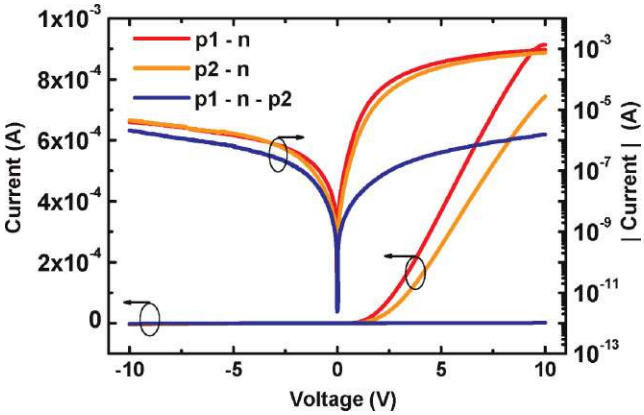

Figure 31 (online color at: www.pss-b.com) Rectifying *I–V* curves of two typical ZnO p–n junctions (red and orange line) on the same substrate, denoted p1–n and p2–n, plotted in linear and logarithmic current scale. In addition, the *I–V* characteristics of these two p-contacts (blue line) is shown, which corresponds to the p1–n–p2 configuration of two opposite p–n diodes. This curve is dominated by the leakage currents of the two diodes.

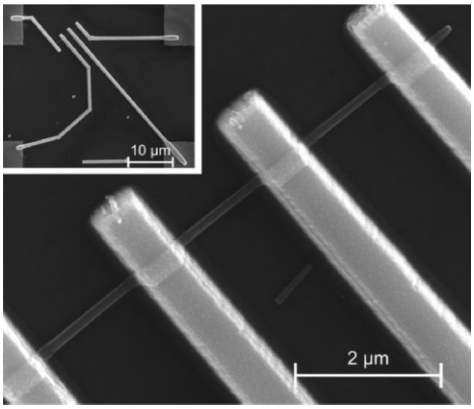

Figure 32 SEM micrograph of a contacted ZnO nanowire. The main image focuses on the contacts whereas the inset depicts the whole structure.

strong indication for the p-type conductivity of our ZnO:P wires.

Because the time between the growth of the first p–n junctions and the electrical measurements is now about 1 year, we can state a corresponding time stability of the ZnO junctions. Finally, electroluminescence experiments with pulsed current excitation (6 V, 8 mA peak current with 1 kHz and 10% duty cycle) on selected junctions showed a very weak, diffuse blue-green light emission. This light emission was visible to the adapted eye in complete darkness.

These results on p-type conductivity of acceptor-doped ZnO nanowires are in line with very few reports in literature. After a post-annealing step, phosphorous-doped ZnO nanowires showed for about 3 months depletion of the source–drain channel current for positive gate voltage, which is clear indication for p-type, hole-related conductivity [51]. Very recently, also nitrogen-doped ZnO nanowires were used as channels in FETs [52]. With 2% N_2O, a p-type I_{DS}-U_G transfer characteristics were measured [51], however no statement about the time stability was given. Very recently, ultraviolet electroluminescence was demonstrated at room temperature from a ZnO rod homojunction light-emitting diode array. The p-type doping was realized by phosphorous ion implantation into defect-free ZnO rods followed by annealing [53].

3.4.2 n-type ZnO:Al wires with controlled carrier concentration In order to fabricate devices with single selected nanowires, new processes are required because the focused ion beam used to built the backgate microwire FETs (see above) cannot be scaled down to nano-dimensions because of the usual micrometer-wide spreading area around the desired IBID metal contacts. Therefore, using the Leipzig FEI Nanolab instrument, an electron beam lithography (EBL) process has been established to produce contacts to single nanowires. The resist is a standard PMMA resist and the metallization can consist of any material or material combination that can be evaporated or sputterd within the standard thin-film processes.

The main difficulty is that the EBL process step itself has to be performed "blind" because the processed nanowire is invisible due to PMMA coverage. Appropriate marking of the substrate structure is necessary for precise alignment during this step. Using this EBL technique, preparation of samples for two- as well as for four-terminal measurements is feasible. An SEM micrograph of a contacted, nominally undoped ZnO nanowire is shown in Fig. 32. Clearly visible are the very well-defined contact pads without any unintentional metal distribution outside the contact pads.

Figure 33 shows an example for electrical measurements on a nominally undoped ZnO-nanowire in bottom-gate FET

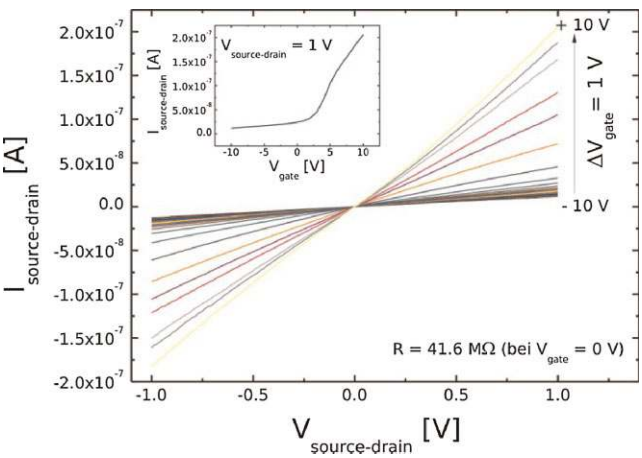

Figure 33 (online color at: www.pss-b.com) $I_{source–drain}$–$V_{source–drain}$ measurements on a nominally undoped ZnO nanowire FET for varying gate voltages V_{gate}. The source and drain contacts are those prepared by the EBL process described above, whereas the Si substrate and its SiO_x layer act as gate electrode and gate oxide, respectively. The inset shows the corresponding transfer characteristics at a source–drain voltage of $V_{source–drain} = 1$ V.

geometry. The *I–V* characteristics at different gate voltages as well as the corresponding transfer characteristics are shown. The graph clearly shows ohmic contact characteristics and the transfer characteristics (inset) confirm the nominally undoped nanorods to be n-type, i.e. full channel depletion for negative gate voltages. Further applications include the fabrication of Schottky type contacts to single nanowires and the characterization of doped nanowires in dependence of the doping level.

3.4.3 Branched nanowires Finally, we show the influence of further dopants as for example Li, Li+N, P, and Mg+P on the morphology of the PLD grown nanostructures. The key for the growth of branched nanostructures is the polar ZnO structure with a Zn-terminated and a O-terminated face perpendicular to the ZnO *c*-axis [7]. If the growth develops under uncompensated surface charges, the spontaneous polarization contributes to increasing continuously the total electrostatic energy, due to the permanent electric dipole inherent to the wurtzite structure. Appearance of branched, and bended, structures minimizes the electrostatic energy on one hand, but increases the total elastic energy on the other hand. This energetic counterbalance between electrostatic and mechanical energies results in the equilibrium structures shown in Fig. 34 for the indicated PLD target compositions.

It has to be noted that the morphology of the depicted branched structures depends critically on the particular growth conditions and the lateral position on the substrate. For the growth of the branched structures in Fig. 34, we applied 15,000 laser pulses with Ar-flow at 100 mbar, 825 °C growth temperature and 2.5 cm distance from target to the substrate front edge.

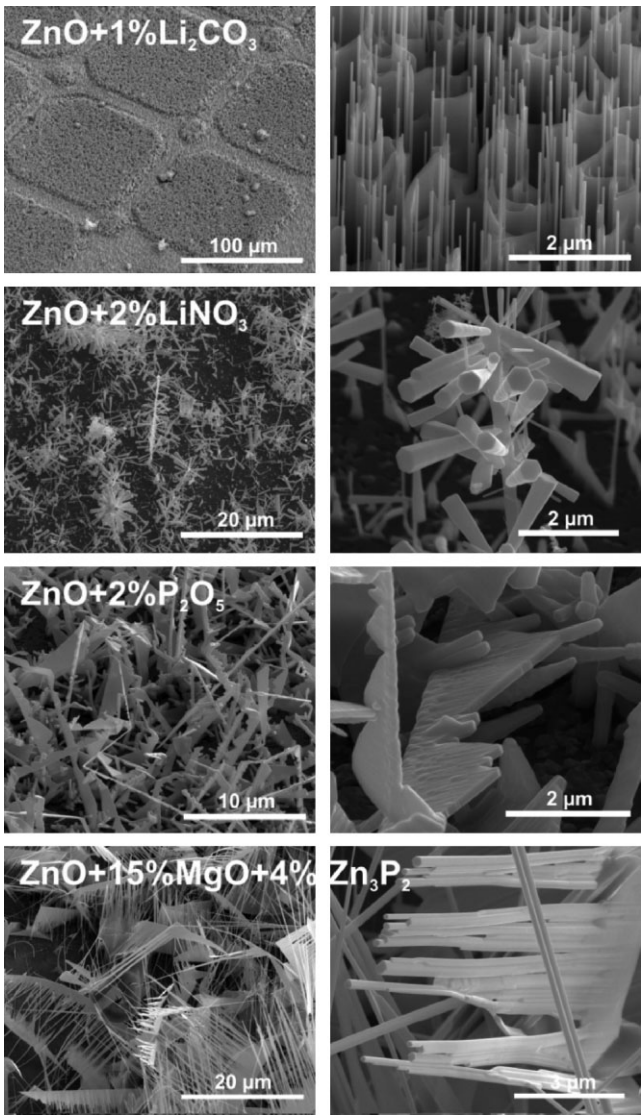

Figure 34 Combinations of one- and two-dimensional, so-called branched ZnO nanostructures as a result of doping with the indicated dopants. The dopant oxide was mixed into the ZnO source target of the high-pressure PLD process. From top to the bottom were obtained: 1D-nanowires on 2D-honeycomb structures; tree-like branched structures; 2D nanosaws; and branched nanocombs. All structures are grown on *a*-plane sapphire substrates using 10 nm Au colloids as nucleation sites.

4 Summary Physical deposition methods as for example a combination of high-pressure and low-pressure PLD for homogeneous nanowire core-shell structures, or direct carbothermal growth of ZnO microwires are very practicable to grow high quality ZnO-based nano- and microstructures. These wires show WGMs and optically excited WGM lasing. The control of the lateral density of the wires was achieved by a ZnO nucleation layer deposited prior to the ZnO nanowire growth by reducing the number of nucleation sites for nanowires. In growth of ZnO/MgZnO core-shell QW structures the axial growth rate of the shell is about three to seven times higher as compared to the radial growth rate. A low-pressure PLD chamber equipped with tiltable and rotateable substrate heater is the key for the improved thickness homogeneity of these coaxial ZnO nanowire Bragg resonators. The above mentioned axial to radial growth rate ratio was found also for these Bragg mirrors which are up to 10 double layers Al_2O_3/yttria stabilized zirconia (see Schmidt-Grund et al.).

The p-type conductivity of phosphorous doped ZnO nano- and microwires was confirmed by three independent indications. Both nano- and microwires show acceptor-related peaks in CL. Furthermore, undoped (n-type) and ZnO:P (p-type) microwires show opposite transfer characteristics of bottom-gate FETs prepared with the wires as channel. ZnO:P nanowire / ZnO:Ga film p–n junctions show rectifying *I–V* characteristics and weak blue-green electroluminescence.

Using EBL, undoped, and doped ZnO nanowires were processed into nanowire FETs to demonstrate the effect of doping on the conductivity of the wire channels. Finally, to demonstrate the huge variability of self-organization, the effect of various dopants on branching of ZnO-based nanostructures is depicted.

Acknowledgements The financial support of the German DFG within research group FOR 522 "Architecture of nano and microdimensional structure elements" is kindly acknowledged. We are indepted to N. Boukos and A. Travlos, National Center for Scientific Research Demokritos, Greece, for TEM investigations. Gabriele Ramm has prepared all source targets and J. Lenzner has produced FE-SEM images.

References

[1] C. Klingshirn, Phys. Status Solidi B **244**, 3027 (2007).
[2] C. Jagadish and S. J. Pearton (eds.), Zinc Oxide Bulk, Thin Films and Nanostructures (Elsevier, Amsterdam, 2006), p. 1.
[3] Y. Xia, P. Yang, Y. Sun, Y. Wu, B. Mayers, B. Gates, Y. Yin, F. Kim, and H. Yan, Adv. Mater. **15**, 353 (2003).
[4] Y. W. Heo, D. P. Norton, L. C. Tien, Y. Kwon, B. S. Kang, F. Ren, S. J. Pearton, and J. R. LaRoche, Mater. Sci. Eng. R **47**, 1 (2004).
[5] S. J. Pearton, D. P. Norton, and F. Ren, Small **3**, 1144 (2007).
[6] H. J. Fan, P. Werner, and M. Zacharias, Small **2**, 700 (2006).
[7] Z. L. Wang, in: Zinc Oxide Bulk, Thin Films and Nanostructures, edited by C. Jagadish and S. J. Pearton (Elsevier, Amsterdam, **2006**), chap. 10.
[8] Y. Mao, T.-J. Park, F. Zhang, H. Zhou, and S. S. Wong, Small **3**, 1122 (2007).
[9] R. S. Wagner, in: Whisker Technology, edited by A. E. Levitt (Wiley-Interscience, New York, 1970), chapter 3
[10] H. F. Fan, W. Lee, R. Hauschild, M. Alexe, G. L. Rhun, R. Scholz, A. Dadgar, K. Nielsch, H. Kalt, A. Krost, M. Zacharias, and U. Gösele, Small **2**, 561 (2006).
[11] S. Kodambaka, J. Tersoff, M. C. Reuter, and F. M. Ross, Science **316**, 729 (2007).
[12] A. Rahm, Growth and Characterization of ZnO-based Nanostructures, PhD thesis, Universität Leipzig (2007).
[13] M. Grundmann, A. Rahm, T. Nobis, M. Lorenz, C. Czekalla, E. M. Kaidashev, J. Lenzner, N. Boukos, and A. Travlos, in: Handbook for Self-Assembled Semiconductor Nanostructures for Novel Devices in Photonics and Electronics, edited by M. Henini (Elsevier, Amsterdam, 2007), chap. 9.
[14] B. D. Yao, Y. F. Chan, and N. Wang, Appl. Phys. Lett. **81**, 757 (2002).
[15] M. Lorenz, J. Lenzner, E. M. Kaidashev, H. Hochmuth, and M. Grundmann, Annalen der Physik (Leipzig) **13**, 39 (2004).
[16] A. Rahm, G. W. Yang, M. Lorenz, T. Nobis, J. Lenzner, G. Wagner, and M. Grundmann, Thin Solid Films **486**, 191 (2005).
[17] B. Q. Cao, M. Lorenz, M. Brandt, H. von Wenckstern, J. Lenzner, G. Biehne, and M. Grundmann, Phys. Status Solidi RRL **2**, 37 (2008).
[18] B. Cao, M. Lorenz, H. von Wenckstern, C. Czekalla, M. Brandt, J. Lenzner, G. Benndorf, G. Biehne, and M. Grundmann, Proc. SPIE Photonics West 2008, Volume **6895**, paper No. 6895-25 (2008).
[19] C. Czekalla, C. Sturm, R. Schmidt-Grund, B. Cao, M. Lorenz, and M. Grundmann, Appl. Phys. Lett. **92**, 241102 (2008).
[20] R. Eason (ed.), Pulsed Laser Deposition of Thin Films: Application-Led Growth of Functional Materials (John Wiley & Sons Inc., Hoboken, New Jersey, 2007).
[21] M. Lorenz, in: Transparent Conductive Zinc Oxide. Basics and Applications in Thin Film Solar Cells, edited by K. Ellmer, A. Klein, and B. Rech, Springer Series in Materials Science, Vol. 104 (Springer, Berlin, 2008), chap. 7
[22] M. Lorenz, E. M. Kaidashev, A. Rahm, Th. Nobis, J. Lenzner, G. Wagner, D. Spemann, H. Hochmuth, and M. Grundmann, Appl. Phys. Lett. **86**, 143113 (2005).
[23] T. Nobis, E. M. Kaidashev, A. Rahm, M. Lorenz, J. Lenzner, and M. Grundmann, Nano Lett. **4**, 797 (2004).
[24] T. Nobis, E. M. Kaidashev, A. Rahm, M. Lorenz, and M. Grundmann, Phys. Rev. Lett. **93**, 103903 (2004).
[25] A. Rahm, T. Nobis, E. M. Kaidashev, M. Lorenz, G. Wagner, J. Lenzner, and M. Grundmann, Proc. Int. Conf. on the Physics of Semiconductors (ICPS-27), Flagstaff, AZ, USA, 2004, edited by J. Menéndez and C.G. Van de Walle, AIP Conference Proceedings **772** (2005).
[26] T. Nobis, E. M. Kaidashev, A. Rahm, M. Lorenz, J. Lenzner, and M. Grundmann, Optical Resonances of Single Zinc Oxide Microcrystals, Proc. Int. Conf. on the Physics of Semiconductors (ICPS-27), Flagstaff, AZ, USA, 2004, edited by J. Menéndez and C. G. Van de Walle, AIP Conference Proceedings **772** (2005).
[27] T. Nobis, E. M. Kaidashev, A. Rahm, M. Lorenz, and M. Grundmann, Proc. of the NATO Advanced Research Workshop 'ZnO as a Material for Micro- and Optoelectronic Applications', in: Zinc Oxide – a Material for Micro- and Optoelectronic Applications, edited by H. Nickel and E. Terukov (Springer, Berlin, 2005), p. 83–98.
[28] T. Nobis, Beobachtung und Modellierung des optischen Flüstergallerie-Effekts in hexagonalen Zinkoxid-Nanoresonatoren, PhD thesis, Universität Leipzig (2006).
[29] A. Rahm, E. M. Kaidashev, H. Schmidt, M. Diaconu, A. Pöppl, R. Böttcher, C. Meinecke, T. Butz, M. Lorenz, and M. Grundmann, Microchim. Acta **156**, 21 (2007).
[30] A. Rahm, M. Lorenz, Th. Nobis, G. Zimmermann, M. Grundmann, B. Fuhrmann, and F. Syrowatka, Appl. Phys. A, Mater. Sci. Process. **88**, 31 (2007).
[31] M. Grundmann, A. Rahm, Th. Nobis, H. Wenckstern, M. Lorenz, C. Czekalla, and J. Lenzner, Proc. MRS **957**, 107 (2007).
[32] J. Zúñiga-Pérez, A. Rahm, C. Czekalla, J. Lenzner, M. Lorenz, and M. Grundmann, Nanotechnology **18**, 195303 (2007).
[33] A. O. Ankiewicz, M. C. Carmo, N. A. Sobolev, W. Gehlhoff, E. M. Kaydashev, A. Rahm, M. Lorenz, and M. Grundmann, J. Appl. Phys. **101**, 024324 (2007).
[34] T. Nobis, A. Rahm, M. Lorenz, and M. Grundmann, Proc. Int. Conf. on the Physics of Semiconductors (ICPS-28), edited by W. Jantsch and F. Schäffler, Austria, Wien, 2006, AIP Conf. Proc. **893**, 1057 (2007).
[35] T. Nobis, A. Rahm, C. Czekalla, M. Lorenz, and M. Grundmann, Superlattices Microstruct. **42**, 333 (2007).
[36] B. Q. Cao, M. Lorenz, A. Rahm, H. von Wenckstern, C. Czekalla, J. Lenzner, G. Benndorf, and M. Grundmann, Nanotechnology **18**, 455707 (2007).
[37] C. Czekalla, J. Guinard, C. Hanisch, B. Q. Cao, E. M. Kaidashev, N. Boukos, A. Travlos, J. Renard, B. Gayral, D. Le Si Dang, M. Lorenz, and M. Grundmann, Nanotechnology **19**, 115202 (2008).
[38] A. O. Ankiewicz, W. Gehlhoff, E. M. Kaidashev, A. Rahm, M. Lorenz, M. Grundmann, M. C. Carmo, and N. A. Sobolev, Proc. Int. Conf. on the Physics of Semiconductors (ICPS-28), Wien, Austria, 2006, edited by W. Jantsch and F. Schäffler, AIP Conf. Proc. **893**, 63 (2007).
[39] M. Mäder, J. W. Gerlach, T. Höche, C. Czekalla, M. Lorenz, and M. Grundmann, Phys. Status Solidi RRL **5**, 200 (2008).

[40] M. Willander, O. Nur, Q. X. Zhao, L. L. Yang, M. Lorenz, B. Q. Cao, J. Zúñiga-Pérez, C. Czekalla, G. Zimmermann, M. Grundmann, A. Bakin, A. Behrends, M. Al-Suleiman, A. El-Shaer, A. Che Mofor, B. Postels, A. Waag, N. Boukos, A. Travlos, H. S. Kwack, J. Guinard, and D. Le Si Dang, Nanotechnology **20**, 332001 (2009).
[41] B. Q. Cao, J. Zúñiga-Pérez, N. Boukos, C. Czekalla, H. Hilmer, J. Lenzner, A. Travlos, M. Lorenz, and M. Grundmann, Nanotechnology **20**, 305701 (2009).
[42] M. Lorenz, B. Q. Cao, G. Zimmermann, G. Biehne, C. Czekalla, H. Frenzel, M. Brandt, H. von Wenckstern, and M. Grundmann, J. Vac. Sci. Technol. B **27** 1693, (2009).
[43] A. O. Ankiewicz, W. Gehlhoff, J. S. Martins, Â. S. Pereira, S. Pereira, A. Hoffmann, E. M. Kaidashev, A. Rahm, M. Lorenz, M. Grundmann, M. C. Carmo, T. Trindade, and N. A. Sobolev, Phys. Status Solidi B **246**, 766 (2009).
[44] C. Kim, W. I. Park, G. C. Yi, and M. Kim, Appl. Phys. Lett. **89**, 113106 (2006).
[45] T. Yatsui, M. Ohtsu, J. Yoo, S. J. An, and G. C. Yi, Appl. Phys. Lett. **87**, 033101 (2005).
[46] S. Heitsch, G. Zimmermann, D. Fritsch, C. Sturm, R. Schmidt-Grund, C. Schulz, H. Hochmuth, D. Spemann, G. Benndorf, B. Rheinländer, T. Nobis, M. Lorenz, and M. Grundmann, J. Appl. Phys. **101**, 083521 (2007).
[47] S. Heitsch, G. Zimmermann, A. Müller, J. Lenzner, H. Hochmuth, G. Benndorf, M. Lorenz, and M. Grundmann, Proc. MRS **957**, 229 (2006).
[48] M. Kim, Y. J. Hong, J. Yoo, G. C. Yi, G. S. Park, K. Kong, and H. Chang, Phys. Status Solidi RRL **5**, 197 (2008).
[49] X. Pan, Proc. 5th Int. Workshop on Zinc Oxide and Related Materials, September 21–24, 2008, Ypsilanti, MI, J. Vac. Sci. Technol. B (2009).
[50] A. Tsukazaki, A. Ohtomo, T. Onuma, M. Ohtani, T. Makino, M. Sumiya, K. Ohtani, S. F. Chichibu, S. Fuke, Y. Segawa, H. Ohno, H. Koinuma, and M. Kawasaki, Nature Mater. **4**, 2 (2005).
[51] B. Xiang, P. Wang, X. Zhang, S. A. Dayeh, D. P. R. Aplin, C. Soci, D. Yu, and D. Wang, Nano Lett. **7**, 323 (2007).
[52] G. D. Yuan, W. J. Zhang, J. S. Jie, X. Fan, J. A. Zapien, Y. H. Leung, L. B. Lou, P. F. Wang, C. S. Lee, and S. T. Lee, Nano Lett. **8**, 2591 (2008).
[53] X. W. Sun, B. Ling, J. L. Zhao, S. T. Tan, Y. Yang, Y. Q. Shen, Z. L. Dong, and X. C. Li, Appl. Phys. Lett. **95**, 133124 (2009).